IOP Publishing Measurement Science and Technology
Meas. Sci. Technol. 31 (2020) 035903 (8pp) https://doi.org/10.1088/1361-6501/ab599f

Super-resolution radially polarized pupil-filtering confocal Raman spectroscopy technology

Shucheng Li[1,3], Lirong Qiu[1,3], Yun Wang[1,4], Han Cui[1,2] and Weiqian Zhao[1]

[1] Beijing Key Lab for Precision Optoelectronic Measurement Instrument and Technology, School of Optics and Photonics, Beijing Institute of Technology, Beijing 100081, People's Republic of China
[2] Division of Biomedical Engineering, James Watt School of Engineering, University of Glasgow, Glasgow G12 8LT, United Kingdom

E-mail: alotrabbits@163.com

Received 16 September 2019, revised 6 November 2019
Accepted for publication 20 November 2019
Published 27 December 2019

Abstract

The spatial resolution of traditional confocal Raman spectroscopy cannot overcome the diffraction limit, which limits its application as a high-spatial-resolution technique. In this paper, a super-resolution radially polarized pupil-filtering confocal Raman spectroscopy (SRPCRS) method is proposed to solve this problem. This method combines confocal Raman spectroscopy imaging technology with radially polarized light compact-focusing technology. The spatial resolution of confocal Raman spectroscopy imaging can be improved by compressing the diameter of the incident spot and by image restoration technology. Simulation and experimental analyses show that this method can increase the spatial resolution of the confocal Raman spectroscopy system to 160 nm when the laser wavelength is 532 nm and the objective lens has an NA of 0.9. This method provides an effective way to achieve high-spatial-resolution confocal Raman spectroscopy images.

Keywords:confocal, high spatial resolution, Raman, radially polarized

(Some figures may appear in colour only in the online journal)

1. Introduction

Confocal Raman spectroscopy combines confocal microscopy and Raman spectroscopy and is widely used as a tool in physical chemistry and biomedical sciences owing to its non-destructive detection, tomography, and molecular fingerprint characteristics [1–7]. Spatial resolution is an important parameter for confocal Raman spectroscopy. In practical applications, a confocal Raman system with high resolution beyond the diffraction limit is often required to get the Raman spectrum image with more information, such as electrochemical performance analysis [8], impurity detection in the ocean [9], the imaging of small molecule in cells imaging [10], follicular thyroid cancer detection [11] and molecular vibration research [12]. However, conventional confocal Raman spectroscopy uses linearly polarized illumination, resulting in a spatial resolution above the diffraction limit. Further, pinholes of sizes of a few hundred microns are used in conventional confocal Raman spectroscopy to ensure micro-spectrum detection sensitivity, which limits its resolution to the micron or sub-micron scale and limits the further improvement of the spatial resolution. Therefore, the improvement of the spatial resolution of confocal Raman spectroscopy systems is a hot topic in the field of Raman spectroscopy.

Several aspects have been studied to improve the spatial resolution of Raman spectroscopy. The super-resolution image restoration method can improve the spatial resolution by recovering the high-frequency information of the Raman spectrum image. Conventional super-resolution restoration methods include the iterative deconvolution [13, 14], regularized deconvolution [15], frequency-domain deconvolution [16], lighting image fusion [17], and Poisson-MAP

[3] Co-first author.
[4] Author to whom any correspondence should be addressed.

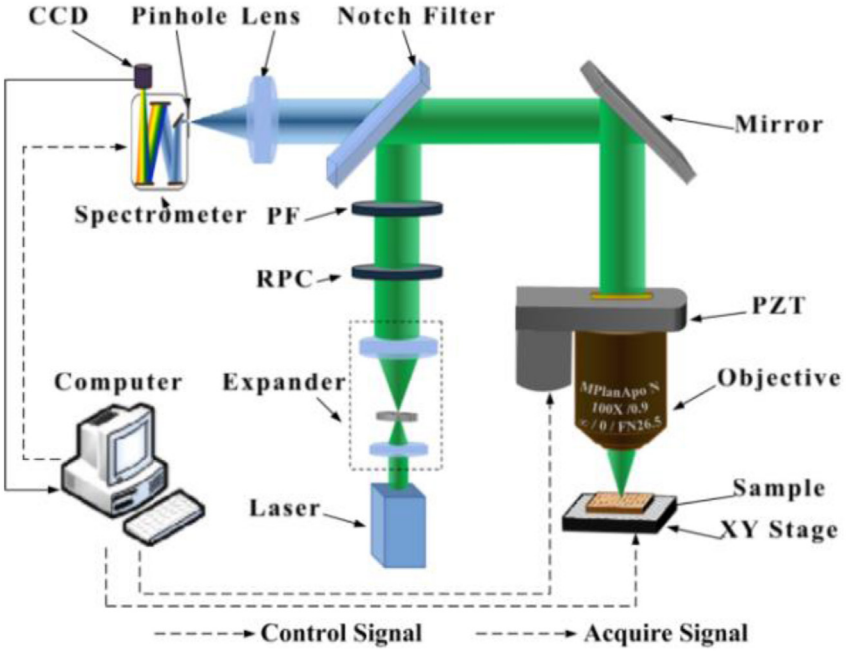

Figure 1. Schematic diagram of RPCRS principle.

super-resolution imaging restoration [18]. These methods can increase the spatial resolution of confocal Raman images by 30%–60%. However, the super-resolution image restoration method is a post-processing method, which cannot improve the spatial resolution of Raman spectroscopy by compressing the diameter of the incident spot and it is easy to generate pseudo-detail information. Therefore, this method is used as an auxiliary means. Several researchers have improved the spatial resolution by changing the optical path of the confocal Raman system. Roider used fiber optics instead of confocal pinholes [19], but this increased the complexity of the optical structure. Malka proposed adding a tunable Fabry–Perot (F–P) filter to achieve the super-resolution spectral lines [20–22]. This method improves the spectral resolution significantly, and can be used in the analysis of the sample components. But it does not discuss the improvement of spatial resolution. The structured light illumination can obtain the high-frequency information of the Raman spectral image by modulating the illumination beam. Among others, it was used by Watanabe, who approached the theoretical limit the confocal Raman system's spatial resolution [23]. Lu proposed scanning pattern illumination microscopy (SPIN), whereby the peak intensity of the excitation light is temporally modulated to double the spatial resolution of Raman spectroscopy compared to traditional wide-field microscopy [24]. However, structured light illumination techniques cannot compress the illumination spot and make the optical path structure more complicated.

In addition to the above methods, the spectral enhancement technique can also improve the spatial resolution of confocal Raman systems by increasing the signal-to-noise ratio of the spectral signal. Surface-enhanced Raman scattering (SRES), tip-enhanced Raman spectroscopy (TERS) and coherent anti-stokes Raman spectroscopy (CARS) are the common spectral enhancement techniques. By combining structured light illumination with SERS technology, Chen achieved a spatial resolution of 120 nm [25]; however, he did not achieve compression of the illumination spot and the substrate preparation was difficult. With TERS, Milekhin achieved a spatial resolution of 2.3 nm [26]. Based on TERS, Zhang used plasmon-enhanced Raman scattering to further improve this spatial resolution [27]. However, TERS does not guarantee the stability and controllability of the needle tip and is difficult to combine with confocal Raman technology. Therefore, it cannot meet the spectral detection of the internal information of samples required in the fields of biology and materials science. By combining photo nanojets injection technology with CARS, Upputuri increased the spatial resolution to 200 nm [28]. Based on this work, Kim [29] used the Torlado-style diaphragm phase filter to further increase the spatial resolution to 130 nm. However, owing to the limitations of CARS, the position and shape of the peaks may change, resulting in complex spectrum analysis and quantitative measurements.

The longitudinal field component of radially polarized light have a ability of compact-focusing when it is focused by a high numerical-aperture (NA) objective. Combined with pupil-filtering technology, the illumination spot can be compressed, which substantially improves the spatial resolution of the system without significantly increasing the complexity of the optical structure. Tang *et al* used this method in confocal microscopy and combined it with image super-resolution technology to increase the spatial resolution of geometric imaging by 32.2% [30].

In this study, a super-resolution radially polarized pupil-filtering confocal Raman spectroscopy (SRPCRS) method is proposed for the first time. This method combines confocal Raman spectroscopy and radially polarized pupil-filtering technology. This method improves the spatial resolution significantly by compressing the excitation spots and confocal

detection of spectrum. In addition, the super-resolution image restoration technique is used to further optimize the obtained Raman spectrum images, thereby further improving the spatial resolution of the confocal Raman spectroscopy system. This method does not contaminate the sample, and can achieve quantitative measurement. It is more practical, and provides a technical approach for the application of confocal Raman spectroscopy for sub-micron measurements.

2. Theoretical principles

The principle of radially polarized pupil-filtering confocal Raman spectroscopy (RPCRS) is shown in figure 1. The laser is converted to RPL by a radial polarization converter (RPC) after passing through the extender. The RPL is then modulated by a pupil filter (PF) and focused by an objective with a high NA on the surface of the sample to generate Raman scattered light. The Raman scattered light is collimated by the objective and is transmitted by a Notch Filter. The transmitted light is focused by a lens into a pinhole in front of the spectrometer and is detected by a spectrometer. The scanning system consists of PZT and *XY* stage. The sample was focused by PZT before scanning the sample. Then the sample is scanned by *XY* stage, and the spectrum is detected by spectrometer. The computer controls the scanning system and acquires spectral signal.

RPCRS systems can be divided into the radially polarized pupil-filtering spectral excitation portion and the confocal Raman spectrum detection portion. The radially polarized pupil-filtering illumination portion compresses the illumination spot and improves the spatial resolution. The confocal Raman spectroscopy detection portion uses a pinhole instead of the entrance slit of spectrometer to further improve the spatial resolution. Therefore, combining these two parts can effectively improve the spatial resolution of the confocal Raman system.

2.1. Radially polarized pupil-filtering illumination analysis

Radially polarized light is a vector beam. Through high NA objective, strong longitudinal field component can be generated at the focal point, and smaller focal spot can be obtained. Therefore, the spatial resolution of confocal Raman system can be improved by using radially polarized light as excitation light. The spatial distribution of point illumination light formed on the object side can be expressed as equations (1) and (2) when RPL illumination is used in the optical path:

$$E_r = 2A\exp\left(\frac{iu}{4\sin^2(\alpha/2)}\right)\int_0^{\alpha}\cos^{\frac{1}{2}}\theta\cdot\sin\theta\cdot\cos\theta \cdot J_1\left(\frac{v\sin\theta}{\sin\alpha}\right)\cdot\exp\left(\frac{iu\cos\theta}{4\sin^2(\alpha/2)}\right)\mathrm{d}\theta, \tag{1}$$

$$E_z = i2A\exp\left(\frac{iu}{4\sin^2(\alpha/2)}\right)\int_0^{\alpha}\cos^{\frac{1}{2}}\theta\cdot\sin^2\theta \cdot J_0\left(\frac{v\sin\theta}{\sin\alpha}\right)\cdot\exp\left(\frac{iu\cos\theta}{4\sin^2(\alpha/2)}\right)\mathrm{d}\theta, \tag{2}$$

where E_r and E_z are the lateral and longitudinal components of the RPL, respectively; ρ is the normalized pupil radius; α is the NA angle of the objective; and A is a constant. Variables u and v are normalized optical coordinates, and can be written as

$$\begin{cases} u = \frac{8\pi}{\lambda}\sin^2\left(\frac{\alpha}{2}\right)\cdot z \\ v = \frac{2\pi}{\lambda}\sin\alpha\cdot r \end{cases}. \tag{3}$$

The object space illumination light intensity distribution is as follows:

$$\begin{aligned} I_{\mathrm{obj}}(v,u) &= \left|E_r^2\right| + \left|E_z^2\right| \\ &= \left|\int_0^{\alpha}\cos^{\frac{1}{2}}\theta\cdot\sin\theta\cdot\cos\theta \cdot J_1\left(\frac{v\sin\theta}{\sin\alpha}\right)\cdot\exp\left(\frac{iu\cos\theta}{4\sin^2(\alpha/2)}\right)\mathrm{d}\theta\right|^2 \\ &\quad + \left|\int_0^{\alpha}\cos^{\frac{1}{2}}\theta\cdot\sin^2\theta \cdot J_0\left(\frac{v\sin\theta}{\sin\alpha}\right)\cdot\exp\left(\frac{iu\cos\theta}{4\sin^2(\alpha/2)}\right)\mathrm{d}\theta\right|^2. \end{aligned} \tag{4}$$

The lateral distribution of the object space with RPL illumination and linearly polarized light (LPL, *x*-direction) illumination are simulated [31, 32]. Their normalized intensity distributions are shown in figure 2.

The lateral intensity distributions of the spot under RPL (figure 2(a)) and LPL (figure 2(b)) illumination are shown in figure 2(c). It can be seen from figure 2(c) that, although the RPL has a strong longitudinal component, the spot is slightly larger than that under LPL due to the influence of the lateral component. In order to compress the spot and lateral component, the pupil is used to modulate the RPL to improve the spatial resolution of Raman spectroscopy.

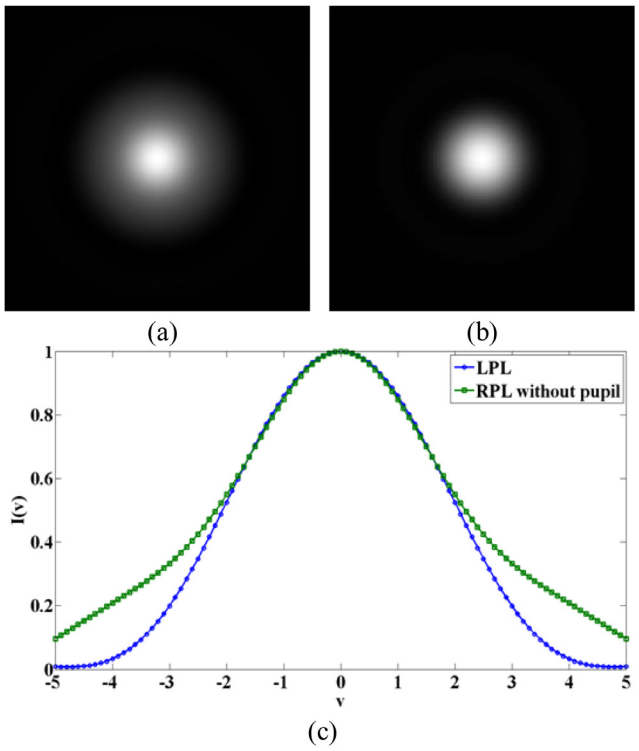

Figure 2. Simulation results of illumination spots of (a) RPL without pupil and (b) LPL. (c) The normalized intensity response curves of different illumination spots.

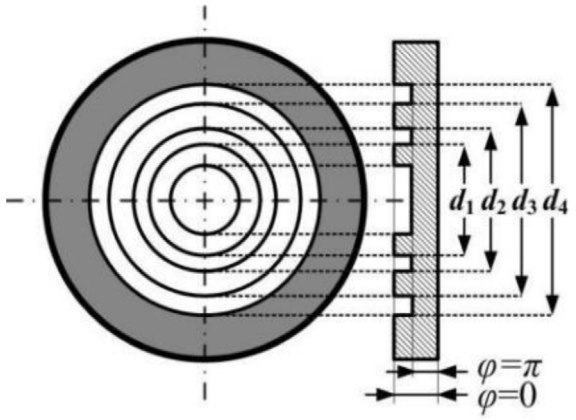

Figure 3. The diagrammatic sketch of the five-zone BOE.

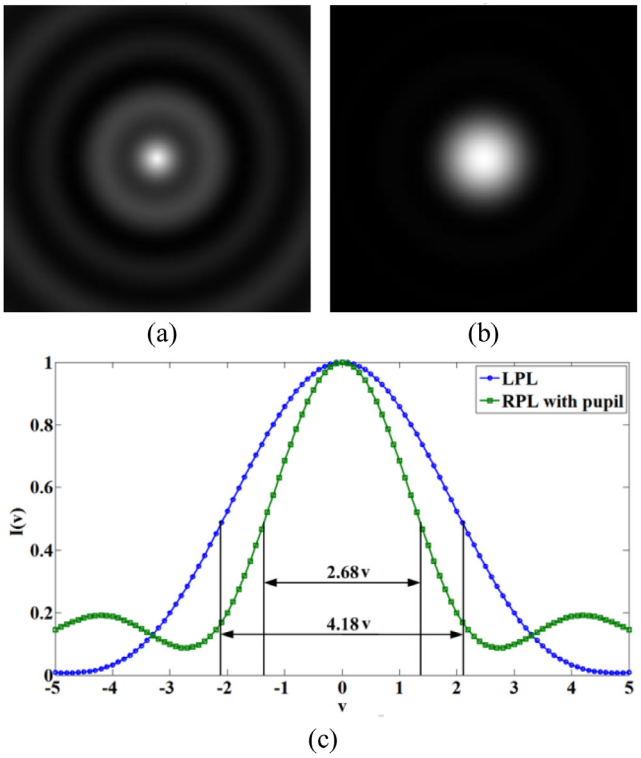

Figure 4. Simulation results of illumination spots of (a) RPL with pupil and (b) LPL. (c) The normalized intensity response curves of different illumination spots.

With the PF, the illumination intensity distribution of the object space is:

$$I_{\mathrm{obj}-P}(v,u)=\left|\int_0^{\alpha}P(\theta)\cdot\cos^{\frac{1}{2}}\theta\cdot\sin\theta\cdot\cos\theta\cdot J_1\left(\frac{v\sin\theta}{\sin\alpha}\right)\cdot\exp\left(\frac{iu\cos\theta}{4\sin^2(\alpha/2)}\right)\mathrm{d}\theta\right|^2+\left|\int_0^{\alpha}P(\theta)\cdot\cos^{\frac{1}{2}}\theta\cdot\sin^2\theta\cdot J_0\left(\frac{v\sin\theta}{\sin\alpha}\right)\cdot\exp\left(\frac{iu\cos\theta}{4\sin^2(\alpha/2)}\right)\mathrm{d}\theta\right|^2,\tag{5}$$

where $P(\theta)$ is a pupil function. Considering the spot size, Stokes ratio, and sidelobe intensity of the system with the PF, a five-zone binary optics element (BOE) was optimized by genetic algorithms to compress the illumination spot and improve the spatial resolution of the imaging system [33].

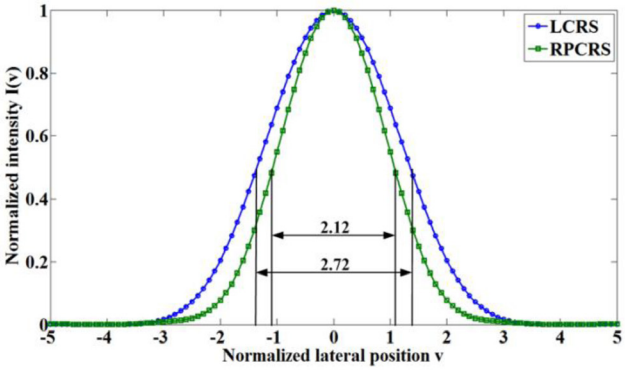

Figure 5. Lateral normalized intensity response curves of RPCRS and LCRS.

When the light wavelength, λ, is 532 nm and the NA of the objective is 0.9, the parameters of the designed five-zone BOE are as follows: radii $d_1 = 0.3731$ mm, $d_2 = 1.6031$ mm, $d_3 = 2.4272$ mm, $d_4 = 3.1488$ mm, and $d = 12.7$ mm and phases $\varphi_1 = \varphi_3 = \varphi_5 = 0$ and $\varphi_2 = \varphi_4 = \pi$. The structure of the designed PF is shown in figure 3.

In this case, the lateral intensity of the object space is simulated and compared with that under LPL. The normalized intensity results are shown in figure 4.

The lateral intensity distributions of the spot under RPL with pupil (figure 4(a)) and LPL (figure 4(b)) are shown in figure 4(c). It can be seen from figure 4 that by using a PF to modulate the RPL, the illumination spot can be compressed effectively. The full-width-at-half-maximum (FWHM) of the illumination spot is used as the spot size. The spot size of RPL with pupil is only 252 nm. Compared with the LPL with a spot size of 394 nm, the spot size of the RPL with pupil is reduced by 35.9%, which indicates a significant improvement in the spatial resolution of the confocal Raman system.

2.2. Analysis of SRPCRS images

To further analyze the spatial resolution improvement of RPCRS imaging, the confocal Raman spectroscopy with radially polarized pupil-filtering illumination is analyzed. For finite-thickness samples, assuming that the Raman spectral radiance is $\sigma(u, v)$, the light intensity distribution in the image space of the RPCRS is

$$\begin{aligned}I_{\mathrm{Raman}}(u,v)&=I_{\mathrm{obj}-P}(u,v)\cdot\left|h\left(\tfrac{u}{\beta},\tfrac{v}{\beta}\right)\right|^2\otimes o(u,v)\\&=\left(\left|\int_0^{\alpha}P(\theta)\cdot\cos^{\frac{1}{2}}\theta\cdot\sin\theta\cdot\cos\theta\cdot J_1\left(\frac{v\sin\theta}{\sin\alpha}\right)\cdot\exp\left(\frac{iu\cos\theta}{4\sin^2(\alpha/2)}\right)\mathrm{d}\theta\right|^2\right.\\&\quad\left.+\left|\int_0^{\alpha}P(\theta)\cdot\cos^{\frac{1}{2}}\theta\cdot\sin^2\theta\cdot J_0\left(\frac{v\sin\theta}{\sin\alpha}\right)\cdot\exp\left(\frac{iu\cos\theta}{4\sin^2(\alpha/2)}\right)\mathrm{d}\theta\right|^2\right)\\&\quad\times\left|\int_{\lambda_{2\min}}^{\lambda_{2\max}}\exp\left(-if_0\tfrac{u}{\beta}\right)\int_0^{\alpha}\cos^{\frac{1}{2}}\theta\cdot\sin\theta\cdot J_0\left(\frac{v\sin\theta}{\beta\sin\alpha}\right)\cdot\exp\left(\frac{iu\sin^2(\theta/2)}{4\beta\sin^2(\alpha/2)}\right)\mathrm{d}\theta\mathrm{d}\lambda\right|^2\otimes o(u,v),\end{aligned}\tag{6}$$

where $\beta = \lambda_2/\lambda_1$, λ_1 is the incident light wavelength, λ_2 is the Raman scattered light wavelength, and $\lambda_{2\min}$ and $\lambda_{2\max}$ are the

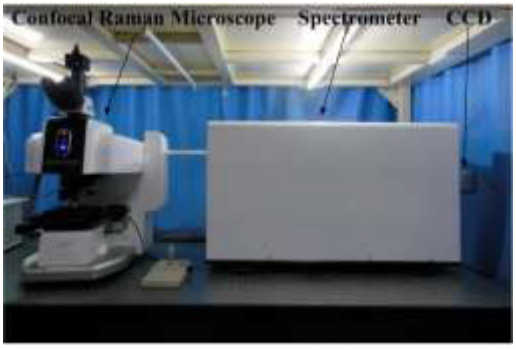

(a)

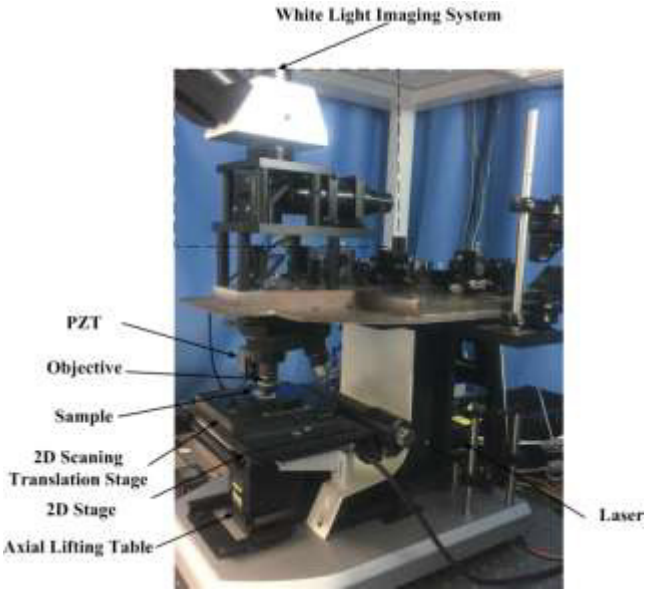

(b)

Figure 6. Setup of SRPCRS.

minimum and maximum wavelengths of the Raman scattered light, respectively.

The laser wavelength used in the experiments was $\lambda_1 = 532\,\text{nm}$. Taking the Raman peak of single-crystal Si at $520.7\,\text{cm}^{-1}$ as an example, which means $\lambda_2 = 547.1\,\text{nm}$, we obtain $\beta = \lambda_2/\lambda_1 = 1.03$. Assuming that $o(\mu,v)$ is the ideal point, equation (6) can be simplified as

$$\begin{aligned} I_{\text{Raman}}(u,v) = \Bigg(& \left| \int_0^{\alpha} P(\theta) \cdot \cos^{\frac{1}{2}}\theta \cdot \sin\theta \cdot \cos\theta \right. \\ & \left. \cdot J_1\left(\frac{v\sin\theta}{\sin\alpha}\right) \cdot \exp\left(\frac{iu\cos\theta}{4\sin^2(\alpha/2)}\right) \mathrm{d}\theta \right|^2 \\ & + \left| \int_0^{\alpha} P(\theta) \cdot \cos^{\frac{1}{2}}\theta \cdot \sin^2\theta \right. \\ & \left. \cdot J_0\left(\frac{v\sin\theta}{\sin\alpha}\right) \cdot \exp\left(\frac{iu\cos\theta}{4\sin^2(\alpha/2)}\right) \mathrm{d}\theta \right|^2 \Bigg) \\ & \times \left| \int_0^{\alpha} \cos^{\frac{1}{2}}\theta \cdot \sin\theta \right. \\ & \left. \cdot J_0\left(\frac{v\sin\theta}{1.03\sin\alpha}\right) \cdot \exp\left(\frac{iu\sin^2(\theta/2)}{4.12\sin^2(\alpha/2)}\right) \mathrm{d}\theta \right|^2. \end{aligned} \tag{7}$$

According to equation (7), when $u = 0$, the lateral intensity response of the RPCRS and linearly polarized pupil-filtering

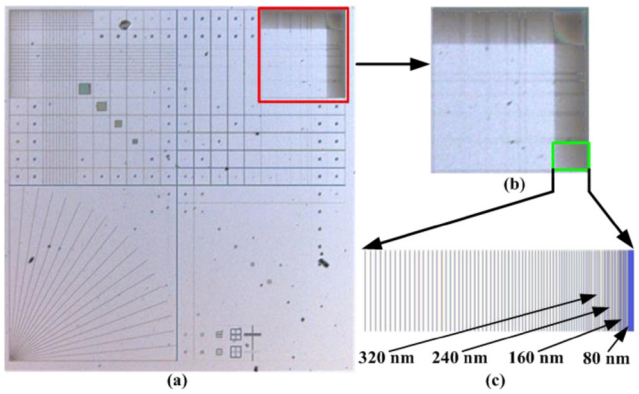

Figure 7. (a) Microscopy observation image of the sample. (b) Zoom-in the area shown in red area of (a). (c) Design image from the area of the green square in (b).

confocal Raman spectroscopy (LCRS) are as shown in figure 5.

It can be seen from the figure 5 that the normalized FWHM of the RPCRS lateral response is 2.12. When the laser wavelength is 532 nm, and the NA of the objective is 0.9, the actual FWHM of the RPCRS is 199 nm. Compared with the LCRS with an FWHM of 259 nm, the RPCRS increased laterally by 23.2%. If the actual FWHM of the lateral response is used as the spatial resolution, RPCRS improves the spatial resolution of the confocal Raman system. As the incident wavelength decreases or the Raman peak of imaging becomes larger, the spatial resolution of the system can be further improved. On this basis, if combined with the super-resolution image restoration method, such as Poisson-MAP super-resolution imaging restoration, SRPCRS can be further proposed.

3. Experimental system and result

3.1. Experimental system

To verify the improvement in the spatial resolution of SRPCRS, an experimental prototype based on figure 1 was developed, as shown in figure 6.

A laser with 532 nm wavelength was used as a light source. The objective lens was a 100× objective lens with an NA of 0.9 produced by Olympus. An S-plate was used to generate the RPL, and the self-designed BOE was made of quartz glass and manufactured by the Chinese Academy of Sciences Institute of Opto Electronics. In order to ensure spectral sensitivity, a pinhole with a diameter of 100 μm was used. The Raman spectrum was acquired by a Czerny-Turner monochromator with a working focal length of 800 mm and CCD by Andor. The sample scanning system consisted of a piezoelectric ceramic transducer (PZT) objective driver and a 2D scanning translation stage produced by PI. The PZT objective driver has a resolution of 0.75 nm, which can be used for high-precision focusing. The 2D scanning translation stage has a resolution of 0.4 nm, so it can be used for scanning with small intervals. The 2D stage and axial lifting table was used to move the sample. In addition, a white light imaging system was used to observe the scanning position of the sample.

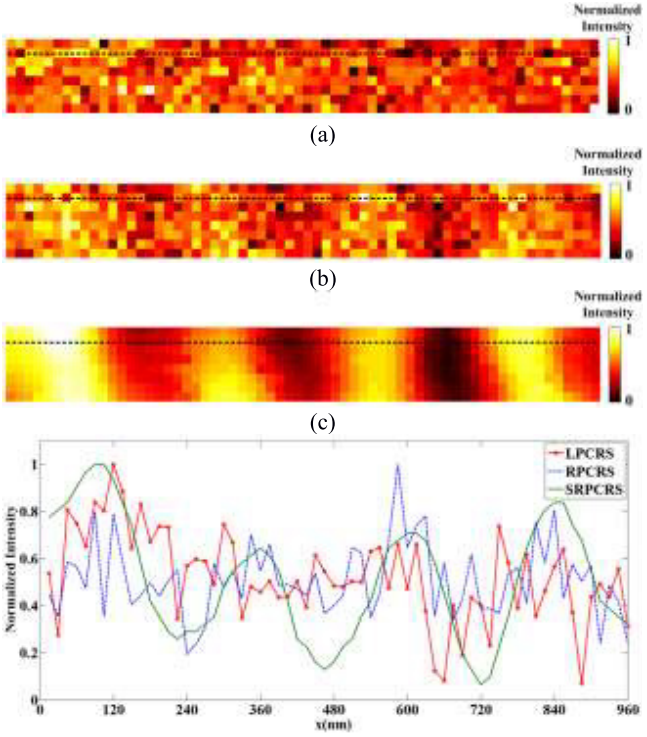

Figure 8. The test image results of vertical bar with 240 nm period (mapping @520.7 cm^{-1}): (a) LCRS, (b) RPCRS, (c) SRPCRS. (d) Representative cross-sectional line profiles taken along the dotted line in (a)– (c).

3.2. Results

The sample shown in figure 7, produced by electron beam lithography, was considered. This is a sub-micron patterned polymethyl methacrylate (PMMA) coated on a Si wafer. Figure 7(a) shows the sample morphology acquired with the microscope (Olympus), figure 7(b) shows the line width pattern of period 80–1000 nm, and figure 7(c) is the design image from the area of the green square in figure 7(b).

RPCRS and LCRS are used to obtain the Raman spectrum of the line-width pattern with a period of 240 nm line width, and the RPCRS image is reconstructed by image restoration technology. The Raman peak at 520.7 cm^{-1} was considered to construct the Raman images with a scan size of 64 × 8 pixels and a lateral scan interval of 15 nm. The entrance slit of the spectrometer has a width of 200 μm and the CCD exposure time is 0.5 s. The obtained test results are compared with the edges, as shown in figure 8.

As can be seen from figure 8, unlike LCRS, RPCRS can obtain a clear periodic reticle morphology of the Raman image and a spatial resolution of 240 nm. When figure 8(b) was restored using Poisson-MAP super-resolution imaging restoration [18], a clearer periodic reticle morphology was achieved, as shown in figure 8(c). It can be seen from figure 8(d) that SRPCRS can obtain a good periodic image and RPCRS can only capture a certain periodic image. In contrast, LCRS can hardly recognize the periodic image of 240 nm.

A line-width pattern with a period of 160 nm was scanned with a scan size of 32 × 4 pixels and a lateral scan interval

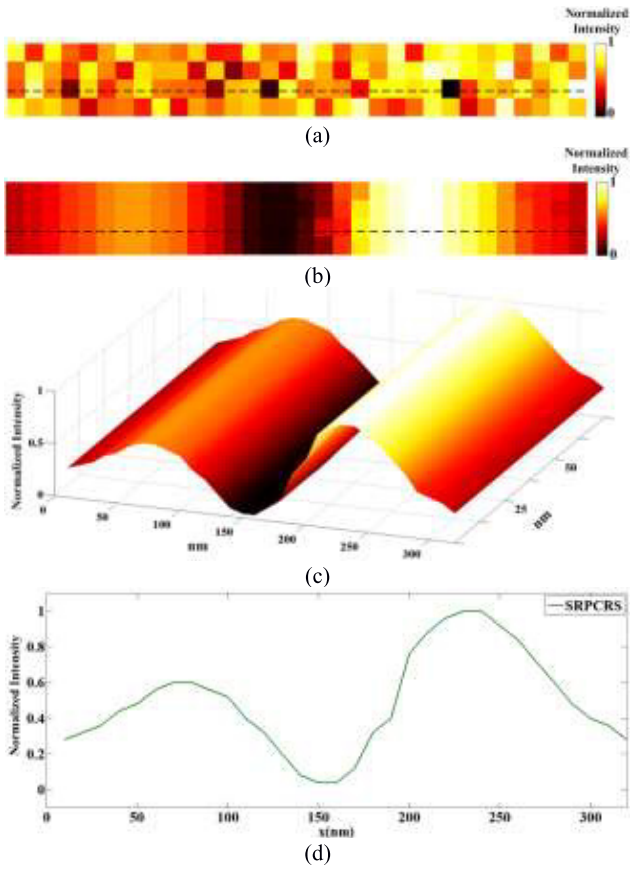

Figure 9. The test image results of vertical bar with 160 nm period (mapping @520.7 cm^{-1}): (a) RPCRS, (b) SRPCRS, (c) 3D image of (b). (d) Representative cross-sectional line profiles taken along the dotted line in (b).

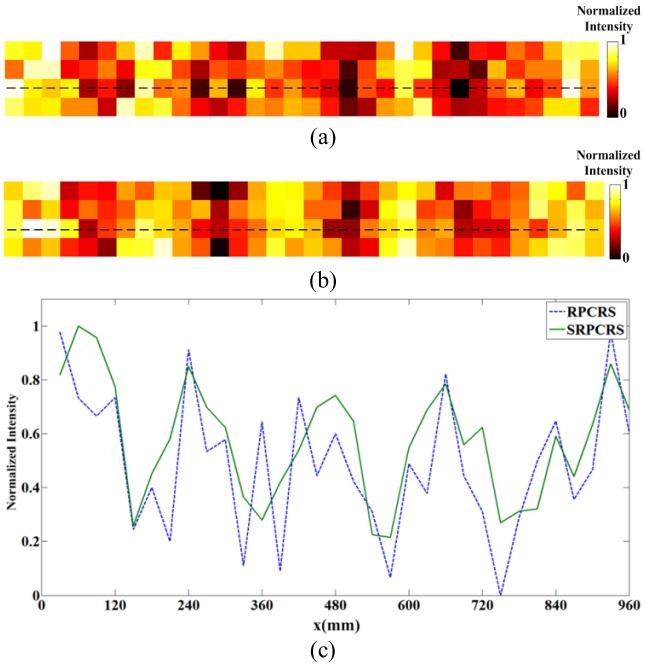

Figure 10. The test image results of vertical bar with 240 nm period (mapping @2953 cm^{-1}): (a) RPCRS, and (b) 3D image of (b). (c) Representative cross-sectional line profiles taken along the dotted line in (a) to (b).

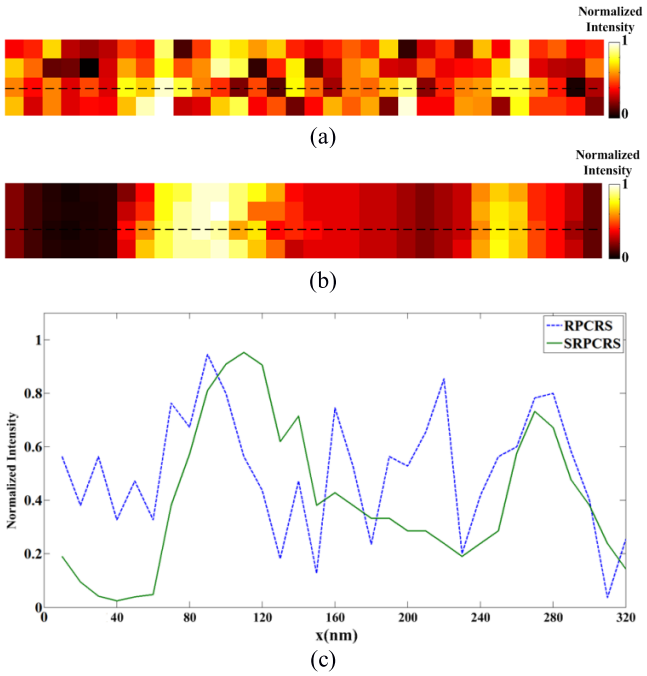

Figure 11. The test image results of vertical bar with 160 nm period (mapping @2953 cm^{-1}): (a) RPCRS, and (b) 3D image of (b). (c) Representative cross-sectional line profiles taken along the dotted line in (a) to (b).

of 10 nm to further verify the ultimate spatial resolution of the SRPCRS system. The entrance slit of the spectrometer has a width of 200 μm and the CCD exposure time is 0.5 s. The result of the RPCRS is shown in figure 9(a), and the results of the SPRCRS are shown in figures 9(b)–(d).

It can be seen from figure 9 that the SRPCRS can recognize the periodic reticle morphology of 160 nm after super-resolution image restoration. On the other hand, LCRS can only recognize the 200 nm periodic reticle by super-resolution recovery [18], indicating the significantly higher resolution of the SRPCRS system.

In order to verify the imaging performance of SRPCRS for different material, the Raman peak at 2953 cm^{-1} of PMMA was used to construct the Raman images. According to the equation (7), when the Raman peak at 2953 cm^{-1} of PMMA is used as the imaging peak position, the spatial resolution of the RPCRS is 198 nm. Therefore, the effect of changes in Raman peak position on spatial resolution can be ignored. RPCRS and SPRCRS are used to obtain the Raman spectrum of the line-width pattern with a period of 240 nm and 160 nm, as shown in figures 10 and 11. The scan size is 32 × 4 pixels, and the lateral scan intervals are 30 nm and 10 nm, respectively.

It can be seen from figures 10 and 11 that when the Raman peak of PMMA is used as the imaging peak position, the RPCRS can recognize the periodic reticle morphology of 240 nm, but it cannot recognize the periodic reticle morphology of 160 nm, so it is consistent with the imaging results with Si. The SRPCRS with image restoration can further improve the contour information of the image, and recognize the periodic reticle morphology of 160 nm, which means SRPCRS can achieve a spatial resolution of 160 nm irrelative to materials.

The spatial resolution of RPCRS is 240 nm, and the spatial resolution of SRPCRS is 160 nm, which means there is a error between the experimental results and the simulation results. This is because that RPCRS only performs focusing by the sharpness method, which easily leads to the defocused of the sample, and causes a decrease in spatial resolution.Besides, if a laser with a shorter wavelength is used, the spatial resolution of the system can be further improved.

4. Conclusion

In this paper, an SRPCRS method is proposed, and its spatial resolution is verified by a self-built experimental instrument. This method uses the radially polarized pupil-filtering technique to improve the spatial resolution of the confocal Raman system, and further enhances the resolution by super-resolution image restoration. Simulation and experimental analyses showed that SRPCRS could achieve a spatial resolution of 160 nm when the laser wavelength was 532 nm and the NA of the objective was 0.9.

SRPCRS provides an effective way to achieve high-spatial-resolution confocal Raman spectral images.

Acknowledgments

The authors would like to thank the National Key R&D Program of China (2018YFF01012001) and National Natural Science Foundation of China (51825501, 61635003).

ORCID iDs

Yun Wang https://orcid.org/0000-0002-9759-5519
Weiqian Zhao https://orcid.org/0000-0003-1986-790X

References

[1] Jiang S, Zhang Y, Zhang R, Hu C, Liao M, Luo Y, Yang J, Dong Z and Hou J G 2015 Distinguishing adjacent molecules on a surface using plasmon-enhanced Raman scattering *Nat. Nanotechnol.* **10** 865–9
[2] Li J, Cai F, Dong Y, Zhu Z, Sun X, Zhang H and He S 2017 A portable confocal hyperspectral microscope without any scan or tube lens and its application in fluorescence and Raman spectral imaging *Opt. Commun.* **392** 1–6
[3] Kallepitis C, Bergholt M S, Mazo M M, Leonardo V, Skaalure S C, Maynard S A and Stevens M M 2017 Quantitative volumetric Raman imaging of three dimensional cell cultures *Nat. Commun.* **8** 14843
[4] Myers G A, Hazra S S, de Boer M P, Michaels C A, Stranick S J, Koseski R P, Cook R F and DelRio F W 2014 Stress mapping of micromachined polycrystalline silicon devices via confocal Raman microscopy *Appl. Phys. Lett.* **104** 191908
[5] Azan A, Untereiner V, Gobinet C, Sockalingum G D, Breton M, Piot O and Mir L M 2017 Demonstration of the protein involvement in cell electropermeabilization using confocal Raman microspectroscopy *Sci. Rep.* **7** 40448

[6] Dresselhaus M S, Jorio A, Hofmann M, Dresselhaus G and Saito R 2010 Perspectives on carbon nanotubes and graphene Raman spectroscopy *Nano Lett.* **10** 751–8
[7] Wu Z, Jiang L, Wang W, Zhao J, Lui H and Zeng H 2019 Precise *in vivo* tissue micro-Raman spectroscopy with simultaneous reflectance confocal microscopy monitoring using a single laser *Opt. Lett.* **44** 1383–6
[8] Wang Y *et al* 2019 Optical methods for studying local electrochemical reactions with spatial resolution: a critical review *Anal. Chim. Acta* **1074** 1–15
[9] Gillibert R *et al* 2019 Raman tweezers for small microplastics and nanoplastics identification in seawater *Environ. Sci. Technol.* **53** 9003–13
[10] Ando J *et al* 2016 High-speed Raman imaging of cellular processes *Curr. Opin. Chem. Biol.* **33** 16–24
[11] Taylor J N *et al* 2019 High-resolution Raman microscopic detection of follicular thyroid cancer cells with unsupervised machine learning *J. Phys. Chem.* B **123** 4358–72
[12] Liu P *et al* 2019 Resolving molecular structures with high-resolution tip-enhanced Raman scattering images *ACS Nano* **13** 9342–51
[13] Govil A, Pallister D M and Morris M D 1993 Three-dimensional digital confocal Raman microscopy *Appl. Spectrosc.* **47** 75–9
[14] Lu W, Chang M, Chen P and Luo W 2014 Iterative deconvolution technique for measurements of diffraction-limited images on optical microscopes *J. Mod. Opt.* **61** S2–9
[15] Tomba J P, Carella J M and Pastor J M 2006 Interphase evolution in polymer films by confocal Raman microspectroscopy *Appl. Spectrosc.* **60** 115–21
[16] Zhang L, Feng X, Zhang W and Liu X 2009 Improving spatial resolution in fiber Raman distributed temperature sensor by using deconvolution algorithm *Chin. Opt. Lett.* **7** 560–3
[17] Wang J, Su R, Richard L, Lu W and Jiang X 2018 A resolution enhancement solution for high-dynamic-range surface topography measurement via lighting image fusion *Opt. Express* **26** 34805–19
[18] Cui H, Zhao W, Wang Y, Fan Y, Qiu L and Zhu K 2016 Improving spatial resolution of confocal Raman microscopy by super-resolution image restoration *Opt. Express* **24** 10767–76
[19] Roider C, Ritsch-Marte M and Jesache Ar 2016 High-resolution confocal Raman microscopy using pixel reassignment *Opt. Lett.* **41** 3825–8
[20] Malka D, Berke B, Tischler Y and Zalevsky Z 2019 Improving Raman spectra of pure silicon using super-resolved method *J. Opt.* **21** 75801–6
[21] Malka D, Berkovic G, Tischler Y and Zalevsky Z 2013 Super-resolved Raman spectroscopy *Spectrosc. Lett.* **46** 307–13
[22] Malka D, Berkovic G, Tischler Y and Zalevsky Z 2015 Super-resolved Raman spectra of toluene and toluene–chlorobenzene mixture *Spectrosc. Lett.* **48** 431–5
[23] Watanabe K, Palonpon A F, Smith N I, Chiu L-D, Kasai A, Hashimoto H, Kawata S and Fujita K 2015 Structured line illumination Raman microscopy *Nat. Commun.* **6** 10095
[24] Lu J, Min W, Conchello J-A, Xie X S and Lichtman J W 2009 Super-resolution laser scanning microscopy through spatiotemporal modulation *Nano Lett.* **9** 3883–9
[25] Chen H, Wang S, Zhang Y, Yang Y, Fang H, Zhu S and Yuan X 2017 Structured illumination for wide-field Raman imaging of cell membranes *Opt. Commun.* **402** 221–5
[26] Milekhin A G, Rahaman M, Rodyakina E E, Latyshev A V, Dzhagan V M and Zahn D R T 2018 Giant gap-plasmon tip-enhanced Raman scattering of MoS_2 monolayers on Au nanocluster arrays *Nanoscale* **10** 2755–63
[27] Zhang R *et al* 2013 Chemical mapping of a single molecule by plasmon-enhanced Raman scattering *Nature* **498** 82–6
[28] Upputuri P K, Wu Z, Gong L, Ong C K and Wang H 2014 Super-resolution coherent anti-Stokes Raman scattering microscopy with photonic nanojets *Opt. Express* **22** 12890–9
[29] Kim H, Bryant G W and Stranick S J 2012 Superresolution four-wave mixing microscopy *Opt. Express* **20** 6042–51
[30] Tang F, Wang Y, Qiu L, Zhao W and Sun Y 2014 Super-resolution radially polarized-light pupil-filtering confocal sensing technology *Appl. Opt.* **53** 7407–14
[31] Hell S and Stelzer E H K 1992 Properties of a 4Pi confocal fluorescence microscope *J. Opt. Soc. Am.* A **9** 2159–66
[32] Richards B and Wolf E 1959 Electromagnetic diffraction in optical systems. II. Structure of the image field in an aplanatic system *Proc. R. Soc.* A **253** 358–79
[33] Wang H, Shi L, Lukyanchuk B, Sheppard C and Chong C T 2008 Creation of a needle of longitudinally polarized light in vacuum using binary optics *Nat. Photon.* **2** 501–5